

Acoustic Fabrication of Living Cardiomyocyte-based Hybrid Biorobots

Jie Wang,[○] Fernando Soto,[○] Peng Ma, Rajib Ahmed, Huaxiao Yang, Sihan Chen, Jibo Wang, Chun Liu, Demir Akin, Kaiyu Fu, Xu Cao, Pu Chen, En-Chi Hsu, Hyongsok Tom Soh, Tanya Stoyanova, Joseph C. Wu, and Utkan Demirci*



Cite This: *ACS Nano* 2022, 16, 10219–10230



Read Online

ACCESS |



Metrics & More



Article Recommendations



Supporting Information

ABSTRACT: Organized assemblies of cells have demonstrated promise as bioinspired actuators and devices; still, the fabrication of such “biorobots” has predominantly relied on passive assembly methods that reduce design capabilities. To address this, we have developed a strategy for the rapid formation of functional biorobots composed of live cardiomyocytes. We employ tunable acoustic fields to facilitate the efficient aggregation of millions of cells into high-density macroscopic architectures with directed cell orientation and enhanced cell–cell interaction. These biorobots can perform actuation functions both through naturally occurring contraction–relaxation cycles and through external control with chemical and electrical stimuli. We demonstrate that these biorobots can be used to achieve controlled actuation of a soft skeleton and pumping of microparticles. The biocompatible acoustic assembly strategy described here should prove generally useful for cellular manipulation in the context of tissue engineering, soft robotics, and other applications.

KEYWORDS: *micro/nano assembly, cardiomyocyte, acoustic, biorobot, external stimuli*



INTRODUCTION

Living cells are ideal robotics building blocks as they do not generate synthetic waste and are biodegradable.^{1–11} Moreover, they exhibit structural robustness, sense complex biological cues, and adapt to environmental changes to rapidly modify their behaviors.^{12–14} For instance, the spontaneous contractile actions of cardiomyocytes^{15–25} and muscle cells^{26–32} can power diverse microdevices such as crawling devices and micropumps, where living cells are used as the engine for intelligent actuators and parts of soft robots.^{24,33–46} Several passive assembly methods^{47,48} (monolayered cell culture or templated fabrication methods) have been widely used to fabricate biorobots due to their simple assembly protocols and scalability. Nevertheless, they face limited design capabilities and delayed establishment of cell–cell interactions due to low packing density. On the other hand, 3D bioprinting methods offer a high degree of design flexibility, although the bioprinting process might entail long fabrication times and result in reduced initial cellular density due to the need of an increased ratio of hydrogel to cell composition required to transfer the materials.^{41,43,49–54} In this direction, there is great potential for biorobotic fabrication methods that can

potentially integrate high cell packing density, rapid fabrication, and design programmability.

Herein, we report the development of acoustic-based programmable active cardiomyocyte-based biorobots in a scalable manner. We previously reported the use of the acoustic assembly of static microparticles and cardiac cells to form predetermined complex structures in different hydrogel systems.^{55–59} Nevertheless, in this work, we expand upon this fabrication method to achieve active biorobots capable of locomotion and performing tasks. Moreover, we demonstrate that cardiomyocytes can be assembled in diverse patterns using Faraday waves and be immobilized into a sacrificial hydrogel that can be removed after the cells secrete extracellular matrix to form a self-structurally stable composite structure. Thus, in comparison to other biofabrication methods that require constant external support or long culture time to form

Received: February 23, 2022

Accepted: May 26, 2022

Published: June 7, 2022



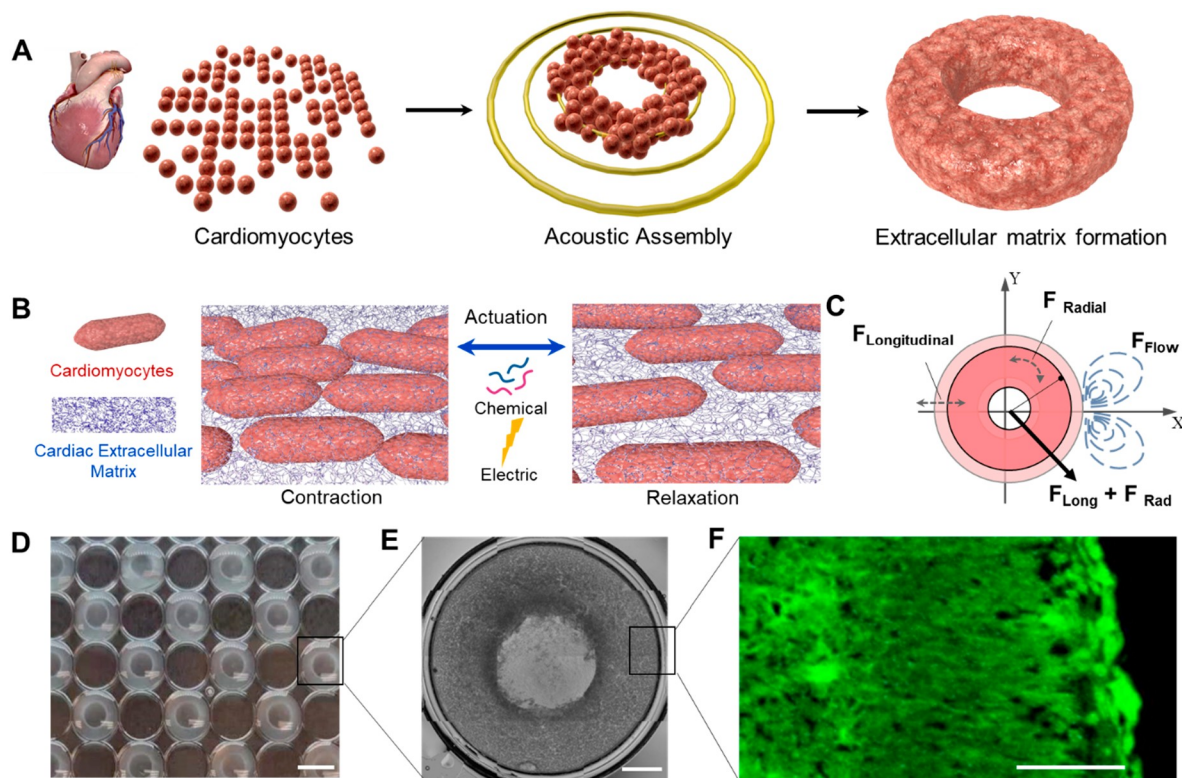


Figure 1. Assembly and actuation of biorobot. (A) Schematic illustration of acoustically driven swarming of multiple cardiomyocytes into a ring-shaped pattern and subsequent extracellular matrix growth (ECM) forming a stable biorobot structure. (B) Scheme of cardiomyocyte contraction and relaxation cycle that results in mechanical actuation of the biorobots. (C) Force diagram generated by the biorobot, including longitudinal force generated by the oriented ECM, radial force generated of cardiomyocytes. (D) Parallel acoustic-driven formation of biorobots in a 96-well plate. The scale bar is 6 mm. (E) Micrograph illustrating brightfield image a full ring-shaped biorobot structure. The scale bar is 1 mm. (F) Fluorescent micrograph illustrating actin (green) showing cardiomyocyte alignment. The scale bar is 800 μm .

organoids, the acoustic assembly method enables the rapid obtention of a highly packed bioassembly that can actuate without the requirement of an external support matrix which might impede efficient actuation. The tight packing of cardiomyocytes can enhance cell–cell contact, interaction, and cell viability by forming gap junctions.⁶⁰ Gap junctions are specialized intercellular channels found in the membranes of neighboring cardiomyocytes that enable the exchange of ions and small molecules between cells to promote cardiomyocyte survival and the formation of anisotropic interactions and cell orientation.⁶¹ We also demonstrate that the assembled cardiomyocyte-based biorobots can be directly interfaced with artificial machines to accomplish force outputs under external modulation, showing promising potential in a wide variety of biomedical fields such as robotics, biohybrid actuation, tissue engineering, and advanced drug screening applications.

RESULTS AND DISCUSSION

We used an engineered acoustic standing waves pattern to generate ring-shaped biorobots, as shown in Figure 1A. A large number of cardiomyocytes (20 million per milliliter) was suspended in a 0.5% w/v alginate solution followed by applying the acoustic field. The acoustic standing wave forces drive the displacement of individual cardiomyocytes forming a controlled ring-shaped swarm. The assembled cardiomyocytes are temporarily fixed by using a sacrificial ionic link hydrogel layer after being sprayed with 150 mM calcium chloride,

responsible for cross-linking the alginate chains into a stable hydrogel. Afterward, the assembled cardiomyocytes immobilized in the hydrogel layer can be peeled from the chamber and transferred into an incubator (Figure S1, Video S1). After 24-h cell culture, cell–cell confinement promotes extracellular matrix release and forms gap junctions between the aggregated cells, providing stability and structural support to the assembled structure. The experimental setup is shown in Figure S2. Next, we removed the sacrificial hydrogel using 55 mM sodium citrate to obtain the cell-only biorobots. The spontaneous cardiomyocyte contraction and relaxation cycle can generate synchronous movement and mechanical actuation of the biorobot, regulated by external chemical and electrical stimuli (Figure 1B). The combined longitudinal and radial forces generated by the biorobot produced and surrounding fluid flow transmitted to nearby surroundings, showing the potential of the biorobot to serve as a mechanical actuator (Figure 1C). We added evenly dispersed cells in wells of a 96-well plate cover and guided them to form a swarm using the acoustic force. The result showed that the cell assembled constructs can be obtained in a large scalable manner (Figure 1D) and the assembled cardiomyocytes construct is uniform (Figure 1E) with aligned actin filaments (Figure 1F).

The acoustic assembly method enables the dynamic assembly as depicted in the schematic and micrograph shown in Figure 2A, where the cell illustrates a time-dependent formative swarm assembly within 3 min. The cells were labeled with cell membrane dye (DiO). ImageJ line tracing of the

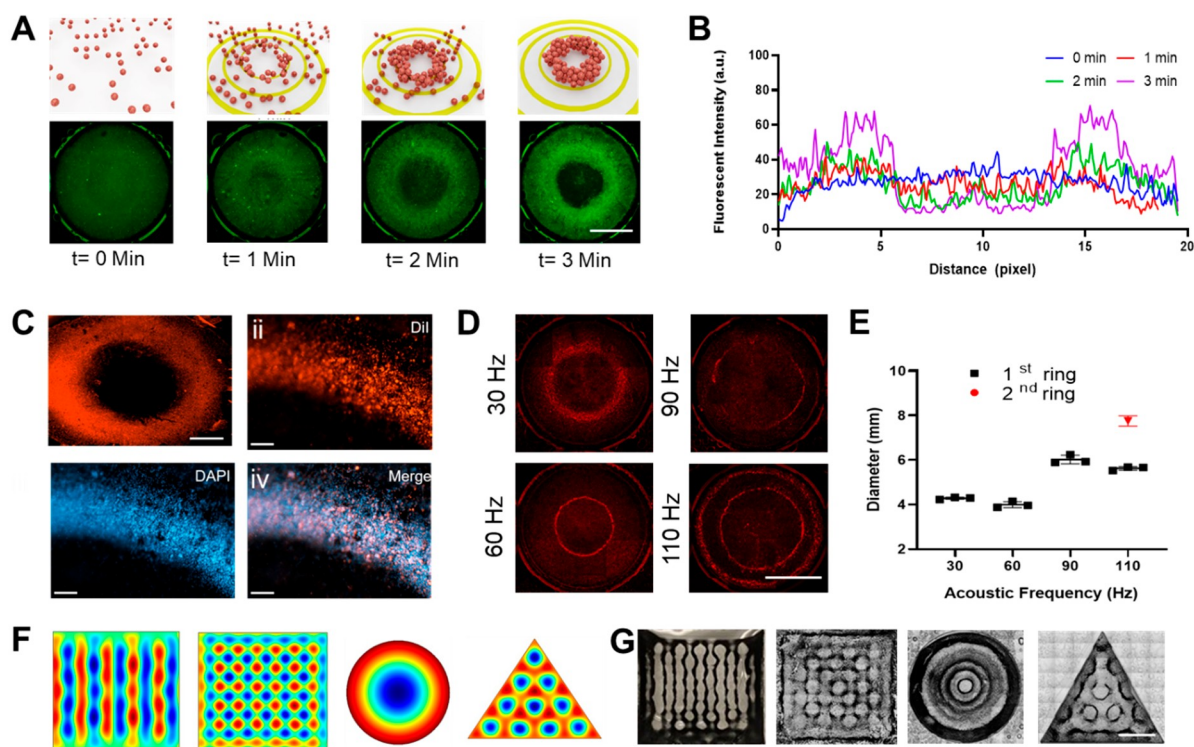


Figure 2. Feasibility and ability to control cell assembly. (A) Fluorescence micrograph showing time-dependent shape morphing fabrication of cell assembly. Cells were labeled with cell membrane dye DiO. The scale bar is 3 mm. (B) The quantitative curve of fluorescent intensity relative to positions at the centerline of B. (C) Fluorescent micrograph of cell nuclei stain (DAPI; ii), cell membrane stain (DiI; iii), and merged image (iv). The DiI staining full ring image in i was different from those in ii–iv. The scale bar is 100 μm . (D) Acoustically assembled cells by different frequencies. The scale bar is 3 mm. (E) The qualitative diameters of the formed cell assembly in D. (F) The numerical simulation results of acoustic assembly and the experimental images (G) of graphene assembled using triangular and square mold geometries. The scale bar is 10 mm.

fluorescent cells was used to measure the accumulation of cardiomyocytes into a ring shape swarm over time (Figure 2B). The swarm can maintain the complete ring shape after staining with red fluorescent cell membrane dye (DiI). The zoomed fluorescent image of the nucleus and membrane showed that the swarm was composed of a high density of closely packed independent cells (Figure 2C).

The diameter of the swarm in our system can be adjusted by the acoustic frequency (Figure 2D). When the frequency reaches 110 Hz, the cells can be assembled into two concentric rings by the acoustic field. The diameter of the rings is shown in Figure 2E, illustrating ring diameters of 4 mm (30, 60 Hz) for low frequencies and 6 mm (90, 110 Hz) for larger ones. To further confirm that our assembly strategy is controllable, we also investigated the collective behavior of synthesized particles under the acoustic field with different frequencies, amplitudes, and templates. Different geometry boundaries (square, triangle, and circle) can result in different acoustic patterns, demonstrating tunable assembly as shown in simulations in Figure 2F. Such tunability is demonstrated experimentally by using graphene powders (diameter of 15 μm) as tracer particles to visualize the acoustic patterns (Figure 2G, Video S2). The swarm patterns can be dynamically reconfigured by adjusting the amplitude and frequency of the sound wave illustrating the dynamic and reversible fabrication methodology. Changes in morphology and shape of the designs can be dynamically directed by finely tuning the applied acoustic frequency as displayed by the different time frames shown in Figure S3 and Figure S4. The numerical simulation of the

deformation, average velocity field, and pressure field generated by acoustic field in a fluid microenvironment is shown in Figure S5. Graphene particles at the bottom of the liquid chamber were driven to the region with a low average force field.

Human-induced pluripotent stem-cell-derived cardiomyocytes (hiPSC-CMs) were cultured following the previously established protocols.^{62,63} We verified the cardiomyocytes' purity using fluorescence-activated cell sorting (FACS) staining and analysis. In this assay, we used the cardiomyocyte marker TNNT2. The cardiomyocytes were detected at around 10% during differentiation (day 12). However, after glucose depletion purification, as expected, most of the noncardiac cells were eliminated, and the remaining purified cardiomyocytes were used solely for the subsequent acoustic assembly experiments (Figure S6). To demonstrate the functional robustness of the biorobot composed of an assembled cardiomyocytes swarm when compared to individual random distributed cardiomyocytes, we generated cardiomyocyte clusters by the random assembly of cardiomyocytes with no acoustic waves and utilized these individual cells with spotty distribution as a control group. Collective cell responses to exogenous cues depend on cell–cell interactions. Cell–cell communication can enhance the sensitivity of cells to external stimuli. Therefore, we first compared the cell-to-cell communication capability between the random individual cardiomyocytes group and the collective ordered cardiomyocytes group. Compared with the random individual cells group, the application of acoustic standing waves resulted in multiple

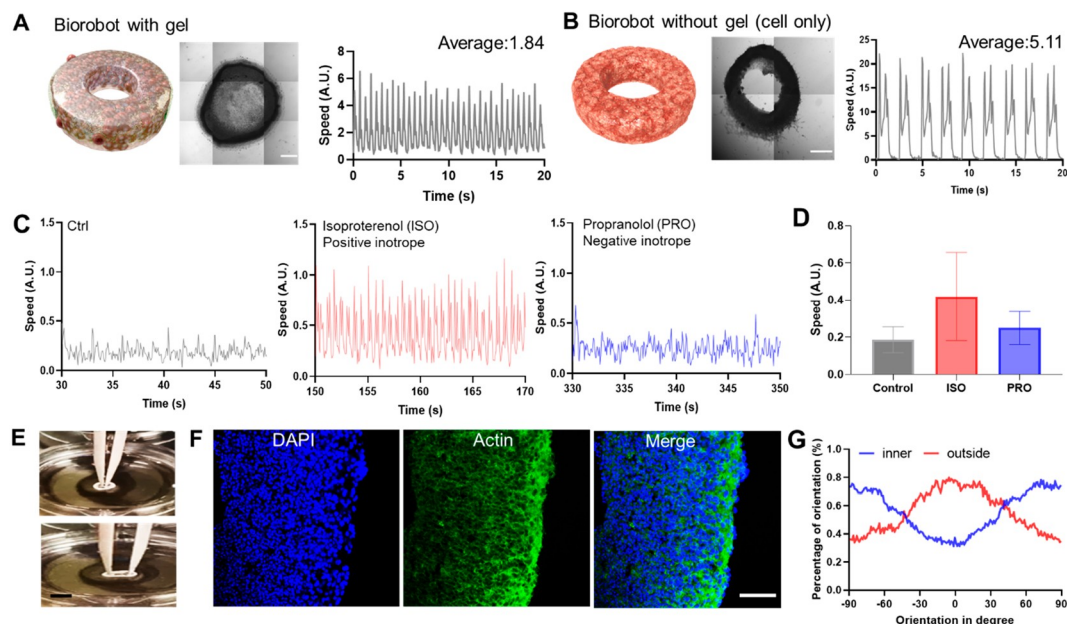


Figure 3. Advantages of template removal strategy and cell alignment inside biorobots. (A) Brightfield image and the quantitative beating speed data of cardiomyocytes assembly before gel release. The scale bar is 1 mm. (B) Brightfield image and the quantitative beating speed data of cardiomyocytes assembly after gel release. The scale bar is 1 mm. (C) The results of speed quantification of biorobots treatment with and without different chemical medications. (D) The quantification summary of C. The error bars represent the standard deviation (SD) value. (E) Images of biorobot before and after tweezer elongation. The scale bar is 1 cm. (F) Fluorescence micrography of biorobot sections. The scale bar is 50 μm . (G) Distribution of actin radial orientation of the biorobot from F.

stacking layers of closely packed cardiomyocytes with strong fluorescent signals from connexin-43. The quantification results confirmed that the intercellular connections in cells residing in the assembled swarm of cardiomyocytes are significantly higher than in random individual cells (Figure S7). It has been reported that cell–cell contact can positively regulate cell viability. On the basis of this concept, we next compared the cell viability of the biorobots composed of assembled cardiomyocytes and random individual cardiomyocytes for a week. The quantification result showed that the cell viability of a biorobot composed of organized cardiomyocytes was $92.32 \pm 2.16\%$, while that of random individual cardiomyocytes was only $75.17 \pm 1.78\%$ (Figure S8). This result illustrates that these independent cardiomyocytes in biorobots can communicate and cooperate to achieve stronger survivability than isolated individual cardiomyocytes in response to external stimuli. We also compared the locomotion ability of biorobots composed of assembled cardiomyocytes and random cardiomyocytes. The average movement speed of the assembled biorobots composed of assembled cardiomyocytes is almost 40 times that of random cardiomyocytes after 24 h of cell culture (Figure S9).

After 1 day of cultivation, the assembled cardiomyocytes are stable by forming connections between closely adjacent cells. Then, we dissolved the Ca-Alg hydrogel using a 55 mM sodium citrate solution for 3 min to obtain biorobots composed of only biological cells. The biorobot assembly does not present spontaneous beating directly after removal of the sacrificial external alginate template. After 2 days of incubation, the biorobots recovered their ability to beat spontaneously. To verify the advantage of our sacrificial hydrogel strategy, we compared the biorobots cross-linked with gel (Figure 3A) and after the gel (Figure 3B) was dissolved. Although the size of our final cell-only biorobots

without synthetic materials support is significantly reduced compared with biorobots encapsulated in the hydrogel, both of them could exhibit intense spontaneous beating. Optical biorobot beating video recordings and force measurements were investigated using the microscope in transmission light mode. The recorded video was processed and analyzed by MYOCYTER macro in ImageJ. Here, the beating speed was characterized by measuring the differences between the successive images of a video using the MYOCYTER. The average spontaneous beating speed of the biorobot with gel was only 1.84 ± 1.36 (a.u.), and the maximum speed was only 6.51 (a.u.). In contrast, the average automatic beating speed of the biorobot without gel could reach 5.11 ± 5.95 (a.u.), and the maximum speed could reach 22.18 (a.u.). This result indicated that the removal of the gel constraint could improve the biorobots' motility, which is beneficial for their performance as actuators.

An ideal robotic engine should be integrated with the characteristics of controllability and versatility under external control.^{64–78} In this direction, we studied the biorobot behavior under external chemical stimulations. We applied isoproterenol (ISO, 1 μM) as a positive inotrope and propranolol (PRO, 1 μM) as a negative inotrope to the biorobot. The biorobot responded to both of these pharmacological agents, with ISO and PRO causing an increase and decrease in the speed of contractile movement, respectively (Figure 3C). The quantification result showed that the average speed of the initial biorobot without any treatment was 0.18 (a.u.). After the addition of ISO for 100 s, the average speed of the biorobot increased to 0.42 (a.u.). In contrast, after the addition of IPO for 100 s, the average speed of the biorobot decreased to 0.25 (a.u.; Figure 3D). We also investigated the chemical drug effect on the contractile movement amplitude of the biorobot. The quantification

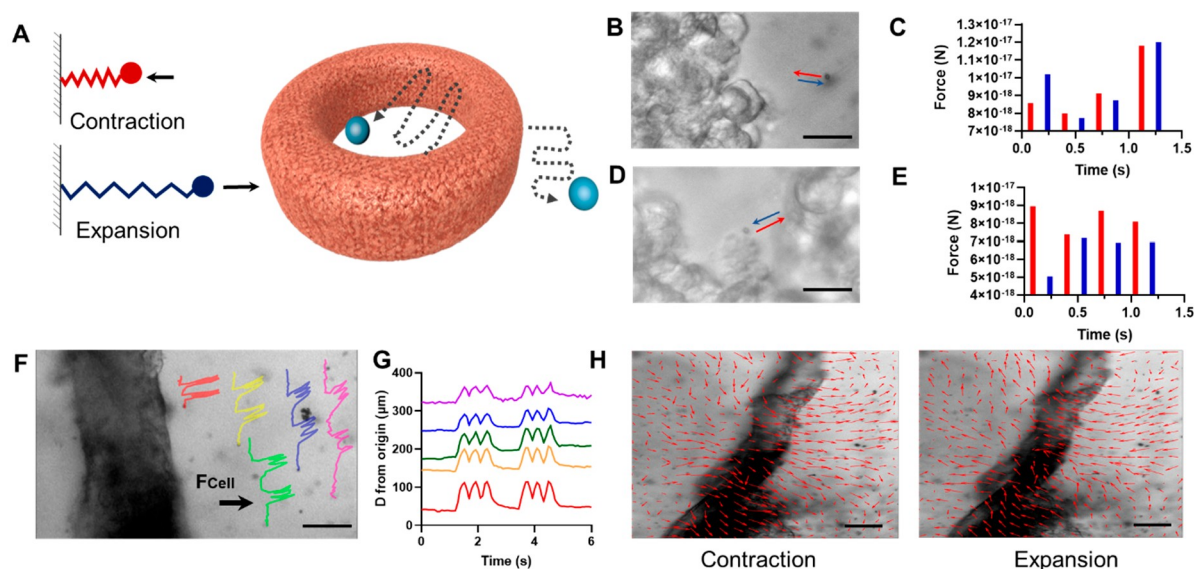


Figure 4. Biorobot-driven manipulation of microbeads. (A) Scheme illustrating force generated by the biorobot produced by contraction (red) and expansion (blue) cycles of the biorobot. (B) Micrograph illustrating the movement of a microbead inside the biorobot. The scale bar is 10 μm . (C) Force generated on the microbead inside the biorobot during four expansion/contraction cycles. (D) Micrograph illustrating the movement of a microbead motion outside the biorobot. The scale bar is 10 μm . (E) Force generated to the microbead outside the biorobot during four expansion/contraction cycles. (F) Micrograph illustrating parallel manipulation of multiple beads illustrates beads displaced by ambient fluid flow and horizontal displacement by a biorobot. The colored lines reflect the actual trajectories of the beads. The scale bar is 100 μm . (G). Horizontal displacement of microbeads over time. (H) Fluid flow vector directions during rest, contraction, and expansion periods, respectively, and the speed gradient fields of microbeads under biorobot actuation. The scale bar is 100 μm .

result showed that the maximum contractile displacement amplitude of the initial biorobot without any treatment was 0.50 (a.u.). After the addition of ISO for 100 s, the maximum amplitude of the biorobot could be increased to 1.00 (a.u.). In contrast, after the addition of IPO for 100 s, the maximum amplitude of the biorobot decreased back to 0.50 (a.u.; [Figure S10](#)). These results showed that the chemical treatments/medications could change the activity of cardiomyocytes and control the movement ability of our soft biorobot, indicating that the biorobot could serve as a drug screening evaluation platform in a simple manner. We also demonstrated that the mechanical properties of the biorobot with strong cell–cell connections were adequate for resisting the repeated stretching action by the tweezers ([Figure 3E](#), [Video S3](#)). We further examined the effect of the gel on long-term viability using Calcein-AM and PI staining protocol. The quantification results showed that the gel-free biorobots exhibited significantly higher cell viability than the biorobots that were fabricated by cross-linking in Ca-Alg hydrogel and remained viable in culture for 14 days ([Figure S11](#)). We inferred that gel removal allows nutrients and oxygen to diffuse better between the cells and allows more intimate contact between adjacent cells without the surrounding gel, which is beneficial to improving cell viability.

Next, we investigated the cell distribution under the influence of acoustic modulation by staining actin filaments of the frozen biorobot section. Fluorescent micrographs illustrate the anisotropic orientation of a biorobot using actin staining, as shown in [Figure 3F](#). The outermost cells were aligned longitudinally to the inner layer. An orientation gradient color map was used to analyze the cell actin orientation of the cell assembly ([Figure S12](#)). Here, the radial direction of the ring was defined to be the vertical direction of

the inner boundary of each position. The percentage of the orientation curve distribution of the inside and outside of the ring-shaped biorobot constructs is complementary ([Figure 3G](#)). This alignment of individual cells inside the biorobots is similar to the highly organized arteries in which longitudinally oriented cells can regulate cell–cell interactions. The circular arrangement of aligned cells can maintain the mechanical strength and vasoactive responsiveness of the vessel structure. There are currently many techniques that can spatially align various cells in high accuracies, such as collagen gel compaction, electromagnetic field, electrospinning of nanofibers, mechanical stimulation, and microstructured-culture-substrates methods.^{79–83} They mainly rely on creating the anisotropy of the environment or uniaxial cyclic strain. However, they usually suffer weak cell–cell interaction and low cell viability with long-term culture because they manipulate uniform suspension and low cell concentration. We demonstrated that a huge number of individual cells could effectively and quickly be aggregated and formed into a ring-shaped swarm. They could also dynamically generate ordered specific geometric arrangement reconfigurations spontaneously to adapt to the surrounding environmental influences induced by the acoustic stimuli. The acoustic force pushes adjacent cells to maintain close contact and form, elongate, and cause cell alignment during the histogenesis via the enhanced cell–cell interactions. The biological driving force can endow soft robots with the ability to mimic the functions of organisms. Unlike most existing biological soft robots, which lack elaborate microarchitecture to induce tissue orientation and realize collaborative motion like live organisms, our biorobots show great potential in simulating the anisotropy architecture and biological performance of the heart.

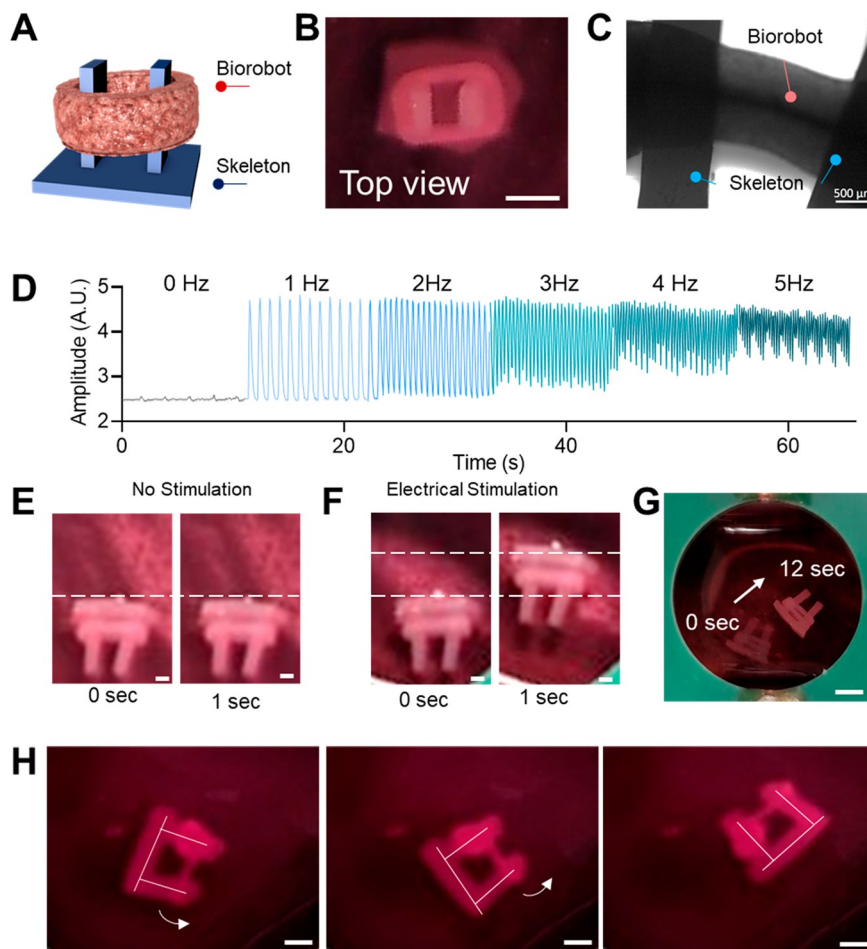


Figure 5. Integration of ring biorobot with soft skeleton actuator. (A) Scheme of biohybrid actuator consisting of ring biorobot and polyurethane soft skeleton. (B) Top view of a photograph of biohybrid actuator. The scale bar is 4 mm. (C) Microscopy image illustrating in more detail the ring surrounding the soft legs of the skeleton. (D) Quantitative analysis illustrating the change in amplitude and frequency of the biohybrid from 0 to 5 Hz. (E) Biohybrid actuator without electrical stimulation. The scale bar is 1 mm. (F) The same actuator with electrical stimulation presenting displacement. The scale bar is 1 mm. (G) Displacement of soft skeleton containing two ring biorobot rings. The scale bar is 5 mm. (H) Rotational motion achieved by the addition of an extra ring in only one leg, inducing asymmetric actuation that results in the illustrated rotational motion. The scale bar is 2 mm.

Next, we studied the cell–cell interactions by immunostaining the biorobot. We selectively stained the gap junctions by connexin 43 to demonstrate the biorobot’s cell–cell communication capability as gap junctions are intercellular channels that not only can allow cell–cell communication through the diffusion of small solutes and ions but also can transfer electrical signals between them for synchronized cardiac contraction.⁸⁴ As shown in Figure S13, the connexin 43 expression signal increased significantly with increasing cell culture duration, further proving the tightening of cell–cell connections over time. We further performed expression profiling by RNaseq of cardiomyocytes used in acoustic fabrication at days 0, 1, 5, 7, 10, and 14 and primary cardiomyocytes without acoustic treatment (control). Functional enrichment analysis of the commonly expressed genes in all day 0, 1, 5, 7, 10, and 14 post-acoustic fabrication and primary cardiomyocytes demonstrated that both groups share similar cardiomyocyte characteristics (Figure S14).

The repeated expansion and contraction cycles of cardiomyocytes induce a tangential flow field that can induce local fluid mixing and collective manipulation of nearby micro-objects as shown in schemes of Figure 4A. To quantify the

external forces generated by the different regions of the cell, we analyzed the trajectory of polystyrene (PS) beads inside and outside the ring-shaped biorobot. We observed that the beads located inside the interior of the biorobot are pushed by direct contact of the ring and fluid forces. (Figure 4B). We statistically quantified the force acting on the microbeads by measuring the force experienced ($F = \text{mass} \times \text{acceleration}$), during each contraction and expansion period of four cycles (~ 1.5 s) as shown in Figure 4C. We attribute the slight variation of force experienced by the microbead to the multidirectional and stochastic force generated by the competition of contact and flow forces in the confined environment of the inner biorobot resulting in a “ping pong” ball motion of the bead (Video S4). In contrast, the bead outside the ring structure experiences unidirectional force generated by the biorobot expansion/contraction cycle, resulting in a more defined spring-like actuation (Figure 4D and Video S4). Similarly, we quantified four cycles of the contraction and expansion forces as shown in Figure 4E, which illustrate the spring back and forward forces experienced by the microbead, thus illustrating that the forces generated by the biorobot can overcome other forces (fluid flow). We have also

demonstrated the ability to induce collective behavior and actuation over a population of multiple active beads displaced by fluid flow. We illustrated the track lines of a group of microbeads moved by ambient flow in the y -axis during the inactive period between contraction and expansion (Video S4). Figure 4F illustrates the track lines of the same group of microbeads after multiple cycles of actuation by the biorobot in the x -axis. Although the contraction of the microstructure can cause a pushing and pulling force on the beads and effectively drive the bead back and forth, the biorobot-induced x -axis displacement on the bead becomes weaker within the longer distance between the bead and the biorobot as shown in the graph in Figure 4G. This is consistent with the stress force distribution of rings; the stress away from the center of the circle is negligible. Nevertheless, regardless of the distance from the ring structure, the parallel actuation occurs simultaneously, as illustrated by the velocity of the beads (Figure S15). To better illustrate the fluid's movement profiles under contraction and expansion cycles, Figure 4H shows the flow vectors generated by the biorobot. Thus, the biorobot shows great feasibility of being utilized as a live soft actuator. It can modify the motion of microparticles surrounding the vessel structure via dynamic fluid pumping motion generated by the beating of the biorobot.

Next, we directly interfaced the cardiomyocyte biorobots with an artificial soft skeleton component consisting of two pillars and a base. We investigated the force outputs produced by a biohybrid design biorobot under external electrical modulation (Figure 5A). We wrapped the ring-shaped biorobot around the elastomer polyurethane skeleton pillars as shown by the actual top view photograph shown in Figure 5B. After another 2 days of normal cell culture, the biorobot started spontaneous beating and could actuate the pillars during expansion/contraction cycles (Video S5). To modulate the cardiomyocyte contraction and thus the skeleton actuation, we used a Grass S88 Stimulator to stimulate the reproducible contraction of cardiomyocytes in biorobots by applying an electrical signal at 0 to 5 Hz (Figure 5C, Video S5 and Figure S16). The use of short-term electrical stimulation, as used here and by others,^{85–87} does not present significant damage to cardiomyocyte tissues, although chronic electrical stimulation could affect the contractile behavior of the cardiomyocytes.⁸⁸

The beating frequency of the biorobot increased with increasing stimulation frequency as shown in Figure 5D and Table S1. The average displacement amplitude of a biorobot without any electrical stimulation was only 2.48 (a.u.), which increased with increased electrical stimulation. We note that the beating amplitude is not linear as the biorobot is stimulated at higher frequencies over 3 Hz due to potentially exceeding the physiological beating limits of cardiomyocytes.

The biorobot ring assembled on a 48-well-plate cover can actuate the soft skeleton without the use of electrical stimuli, but no dynamic propulsion or displacement is present (Figure 5E). On the other hand, applying electrical stimuli resulted in an increased beating frequency that leads to actual displacement in the direction of the head of the soft skeleton (Figure 5F and Video S6). Moreover, we tested the addition of more biorobot rings to evaluate the effect on locomotion. When introducing a second ring, the structure moves toward the legs (Figure 5G). Rotation was achieved by placing an additional ring only on one of the legs of the soft skeleton apart from the initial one covering both legs, this resulted in rotational motion (Figure 5H and Video S7). In addition, to provide a

benchmark for recently developed biorobots in the field, we compared the speed and size of these organoids (Table S2).^{9,20,24,26,27,39,42} The quantitative speed of the biorobot is 0.7 mm/s at 5 Hz simulation. The main benefits of fabricating biorobots via acoustic assembly is that it generates highly packed cell assemblies. Briefly, our acoustic assembly method provides close packing of cells at high density which promote easier contact between cells.

The beating of the legs produces localized fluid streams that could be custom-tailored to produce mixing in a biocompatible and autonomous manner, as shown by overlap images of displaced tracer beads in Figure S17 and Video S7. We observed the continuous actuation of the biorobot for periods up to 4 h during experimentation. Moreover, the biorobots are expected to actuate as long as optimal environment conditions (glucose, temperature, CO₂ and pH) are available.^{61,89} The integration of active biological assemblies and synthetic structures could assist in the design of biorobots.

CONCLUSION

In this study, we developed a method to produce highly scalable, biorobots with collective synchronous behavior, comprised of millions of metabolically active living cells. A single vibration generator generates the acoustic fields that direct the assembly of cells into engineered biorobots. The assembly structure can be tailored by fine-tuning relevant parameters such as chamber geometry, frequency, and amplitude. Adjacent independent cells in the assembly can actively communicate through their own secretions, without the need for any surface modification. The resulting biorobot presents autonomous beating that can be used as an actuator and respond to other external stimuli (e.g., chemicals). The integration of cardiomyocytes with synthetic backbones has been used to develop capabilities other than locomotion, such as morphology and optical properties. Here, we demonstrated the biorobots can be integrated with synthetic skeletons to serve as a hybrid self-powered soft actuator and manipulate other microscale artificial objects. Future work will aim to make use of diverse acoustic patterns that can be integrated with previously reported biohybrid skeleton designs (springs, cantilevers, jellyfish, and stingrays) to achieve specific types of behavior, e.g., grabbing objects, mixing fluid, or self-displacement. The biorobot approach presented here leveraged the performance robustness and autonomy of living cells/tissues as biorobot actuators successfully, which could play a significant role in advancing the progress in soft robotics and tissue engineering for the realization of microscale biohybrid actuators.

METHODS

Cell Culture. The murine fibroblast cell line NIH 3T3 was purchased from the American Type Culture Collection (ATCC, Manassas, VA). Supplemented with 10% (v/v) FBS and 1% (v/v) antibiotic, the Dulbecco's Modified Eagle's Medium (DMEM) was used to maintain the NIH 3T3 cells. Human origin-induced pluripotent stem-cell-derived cardiomyocytes (iPSC-CMs) were kindly provided by the Dr. Joseph C. Wu lab at Stanford University, with the protocols approved by the Stanford University Institutional Review Board (IRB). The hiPSC-CMs were differentiated from hiPSC (No. SCVI 273 from Stanford CVI biobank) according to their previous CHIR/IWR-1 based protocol reported in our previous work.^{62,63} The hiPSC-CMs were purified by the glucose starvation approach starting at differentiation day 9 for 4 days to reach a purity of 90% to 95% (cardiac troponin-T positive). Accordingly, there were

5% to 10% noncardiac cells in the purified hiPSC-CMs that were negative in the endothelial marker of vWF and fibroblast marker of P4HB and slightly positive in the proliferation marker of ki67.⁶³ Moreover, since we used the serum-free cell culture medium (RPMI with B27 plus insulin) for the hiPSC-CM culture and biorobot fabrication and maintenance, the effect from the noncardiac cells on the biorobot performance was minimal supplemented with 4% (v/v) FBS and B27 with insulin (Life Technologies); the RPMI medium was used to maintain iPSC-CMs. All of the cell cultures were incubated in a humidified cell culture chamber at 37 °C in a 95% air/5% CO₂ atmosphere, and the medium changed every other day.

Fabrication of Biorobot. The acoustic assembly device for patterning individual cells into a biorobot with a predetermined configuration is composed of an arbitrary function generator (33500B, Agilent, USA), a vibration exciter (US6001, 3B Scientific, USA), and an audio power amplifier (Lepai LP-2020A+, Parts Express). For graphene oxide assembly, we used a PMMA chamber with a designed shape made by laser cutting. For cell assembly, we used the cover of a commercial 96- or 48-well plate as the acoustic chamber and put it onto the vibration exciter. We resuspended the isolated cells in a saline solution containing 0.5% (w/v) alginate, then we added this cell suspension (50 μL, 2M) into each well of the plate cover. The AC amplitude we applied for the acoustic stimuli was 22 mVpp, and the frequency was 55 Hz. After it formed the biorobot visually, we sprayed 150 mM calcium chloride solution from above the plate cover to immobilize the biorobot in the hydrogel for 10 s. Next, we peeled off the biorobots using a stainless microspoon (Bel-Art F36705-0000, Global) and transferred them to a cell culture incubator. After normal cell culturing overnight, we added sodium citrate solution (55 mM) to dissolve the gel to obtain cell-only biorobots. The biorobots do not present spontaneous beating upon release from the hydrogel, but after 2 days of incubation they recover their ability to beat.

Biorobot Analysis. All chemical reagents were purchased from Sigma-Aldrich unless otherwise noted. Biorobot was fixed in 4% (v/v in PBS) paraformaldehyde for 2 h, rinsed using PBS (3 × 30 min), and cryoprotected in 30% sucrose in PBS overnight. After embedding the samples in molds with optimal cutting temperature (OCT) medium (Tissue-Tek; Miles Inc., Elkhart, IN), the biorobot was frozen in dry ice and stored at −80 °C before sectioning. Parallel sections of the biorobot with a thickness of 14 μm were cut on a cryostat (Leica CM 1850; Leica Biosystems, Wetzlar, Germany). Sections were stained with hematoxylin and eosin (H&E) for structural analysis. For the immunofluorescence staining-based cellular connections study, sections were washed with PBS before being permeabilized with 0.3% triton-X100 (Sigma-Aldrich) for 5 min at 4 °C. Sections were next blocked in 1% BSA solution (blocking solution) for 1 h at room temperature following a 1:200 dilution of anti-connexin43 antibody (Thermo Fisher Scientific, 71-0700) overnight at 4 °C in the blocking solution. Next, the biorobot was washed with PBS then incubated for 1 h at room temperature in the dark with 1:200 Goat Anti-Rabbit IgG H&L (Alexa Fluor 594, Abcam, ab150080) in the blocking solution. For the study of actin orientation within the biorobot, sections were immersed in 1:50 Alexa Fluor 488 Phalloidin (ThermoFisher Scientific, A12379) for 1 h at room temperature. Subsequently, biorobots were washed with PBS, and cell nuclei were stained with DAPI (Life Technologies, D1306) in PBS. Actin orientations were analyzed using the OrientationJ plugin in ImageJ (NIH). A color map, orientation distribution curve, and coherency degree were generated with local window $\delta = 1$ pixel. A total number of $n = 3$ samples were analyzed for each quantification. The biorobots' beating behavior was evaluated for different periods ranging from a few minutes to 4 h, where the behavior of the ring beating did not vary significantly. To evaluate the cell viability, the biorobots were washed with PBS and incubated in 2 mL of prewarmed PBS containing 1.5 μL of calcein-AM (1 mM) solution for 20 min at 37 °C. Later, we removed the staining solution and added 2 mL prewarmed PBS containing 50 μL of PI (2 mg/mL) solution and incubated for 5 min at room temperature. We removed the staining solution and washed twice for 5 min in PBS at 37 °C and took the construct for imaging under a Zeiss AxioObserver Z1

microscope using a 5× objective. We captured images in the green (488 nm) and red (570 nm) channel and assessed the viability percentage using ImageJ. We counted the live cells with a green label and dead cells with a red label as well as colabelled with green and red. Cell number was acquired by counting cells in each focal plane (in focus) to get the sum. A total number of $n = 3$ samples were analyzed for each quantification.

Motion Behavior Studies of Biorobots. First, 1 μM isoproterenol (ISO, Sigma-Aldrich) and 1 μM propranolol (PRO, Sigma-Aldrich) were dissolved in H₂O. Optical biorobot video recordings and force measurements were investigated using the microscope in transmission light mode. The recorded video was processed and analyzed using MYOCYTER macro, with FIJI version 2.0.0-rc-69/1.52n of ImageJ. "Speed" represents the differences between the successive images of a video and indicates the speed of a movement. "Amplitude" represents the difference between every single frame and the reference frame. The bead velocity was measured by using the MJ track plugin for ImageJ. We note that all speed measurements were done manually. Thus, there is an inherent bias measurement by each user to quantify this value. We measured five times the displacement of the same particle over 79 frames. When comparing the x displacement, we obtained an average standard deviation of 0.24 μm by averaging the standard deviation for each point frame. When conceding the path length of the same particle, the measurements yielded an average of 225.07 ± 2.91 μm or 1.2% error by the user. This measuring variation is relatively small and does not affect any conclusion based on their quantitative analysis. The force was calculated using force = mass × acceleration, where the acceleration values were taken using the MJ track as previously mentioned; the density of each polystyrene bead (1055 kg/m³) was multiplied by the volume of the 2 μm of each bead. The microscope recording frame rate was 14 frames per second.

Fabrication of Ring-Shaped Bioactuator. The skeleton for the bioactuator was fabricated by pouring a polyurethane commercial mix (Ecoflex 0–30) over a PDMA template consisting of two legs and a base. The material was cured at 65° over 30 min and washed to remove noncured materials. Next, the acoustic fabricated ring-shaped biorobot assembled on a 48-well-plate cover was placed over the legs of the soft skeleton. Square monophasic pulses are applied to the cardiomyocytes through a Grass S88 Stimulator for electrical stimulation. The carbon plates were placed across the cell culture dish with an electrode distance of 3 cm and then connected to the stimulator of the completion of the circuit loop. Electrical stimulation was generated across the cell culture with optimized stimulation conditions, such as the pulsed electrical field, pulse frequency, and pulse duration. In this study, for experiments of electrically stimulating biorobots, which were acoustically assembled from cardiomyocytes (30 M/mL), the optimized parameters were a pulse duration of ~5 ms, a frequency of 1 to 5 Hz, and field intensity of 5 V/cm. We monitored the motion of biorobots through the phone with a built-in camera or bright field microscope. Then, all images and videos were analyzed using ImageJ to obtain the effect of electrical stimulation on biorobots.

Finite Element Analysis of Faraday Wave. Finite element analysis was conducted to characterize the patterning of graphene particles under Faraday standing waves. The Faraday waves were generated at the air–liquid interface with a fixed boundary in a chamber, and it could be considered to be caused by body force F generated by a sinusoidal acceleration signal applied to the exciter, which can be written as

$$F = a \times \rho \quad (1)$$

$$a = a_{\text{max}} \cos(4\pi ft) \quad (2)$$

in which ρ is the density of the fluid, a_{max} is the maximum acceleration applied to the exciter, and f is the working frequency of the exciter. The Faraday wave can be simulated by applying this external force when solving the governing equation of the dynamic flow motion. These governing equations refer to the Navier–Stokes equations, which can be written as

$$\rho \frac{\partial V}{\partial t} = F + \rho g - \nabla p + \mu \nabla^2 V \quad (3)$$

in which V is the velocity vector of the flow field, F is the body force in eq 1, μ is the dynamic viscosity of the fluid, and g is the acceleration of gravity.

All of the simulations were performed using finite element-based computational software (COMSOL Multiphysics). To reduce the computational cost and build the physical model correctly, we simplified the modeling. “Laminar Flow” physics was used to solve the governing equations of dynamic fluid motion, and the deformation of fluid motion was handled by adding a “dynamic mesh” condition. The “volume force” condition was applied to the 3D calculation domain of “Laminar Flow” physics. The boundary conditions on the air–liquid interface and solid–liquid interfaces were set to “free surface” (surface tension of gas–liquid interface σ) and “no-slip”, respectively. The problem was solved via a “time-dependent” solver. The parameters of materials used in the calculations are given below: the dynamic viscosity of the fluid (μ) was 1.01×10^{-3} Pa·s; the surface tension of the gas–liquid interface (σ) was 72.8 mN/m; the working frequency of the exciter (f) was 80 and 100 Hz; the maximum acceleration applied to the exciter (a_{\max}) was 5g and 6g; and the acceleration of gravity (g) was 9.80 m/s².

ASSOCIATED CONTENT

Supporting Information

The Supporting Information is available free of charge at <https://pubs.acs.org/doi/10.1021/acsnano.2c01908>.

Additional figures and expanded fabrication and characterization of the biorobot (PDF)

Acoustic assembly of biorobot (MP4)

Fabrication of different geometrical acoustic patterns (AVI)

Examination of biorobot mechanical resiliency (AVI)

Biorobot-driven manipulation of microbeads (AVI)

Integration of biorobot with soft skeleton (AVI)

Propulsion of biorobot under electrical stimuli (MP4)

Rotation of biorobot under electrical stimuli (AVI)

AUTHOR INFORMATION

Corresponding Author

Utkan Demirci – *Bio-Acoustic MEMS in Medicine (BAMM)*
Laboratory, Canary Center at Stanford for Cancer Early Detection, Department of Radiology, School of Medicine Stanford University, Palo Alto, California 94304-5427, United States; *Canary Center at Stanford for Cancer Early Detection, Department of Radiology, School of Medicine, Stanford University, Palo Alto, California 94304-5427, United States*; orcid.org/0000-0003-2784-1590;
Email: utkan@stanford.edu

Authors

Jie Wang – *Bio-Acoustic MEMS in Medicine (BAMM)*
Laboratory, Canary Center at Stanford for Cancer Early Detection, Department of Radiology, School of Medicine Stanford University, Palo Alto, California 94304-5427, United States; *Canary Center at Stanford for Cancer Early Detection, Department of Radiology, School of Medicine, Stanford University, Palo Alto, California 94304-5427, United States*; orcid.org/0000-0003-2223-5794

Fernando Soto – *Bio-Acoustic MEMS in Medicine (BAMM)*
Laboratory, Canary Center at Stanford for Cancer Early Detection, Department of Radiology, School of Medicine Stanford University, Palo Alto, California 94304-5427, United States; *Canary Center at Stanford for Cancer Early*

Detection, Department of Radiology, School of Medicine, Stanford University, Palo Alto, California 94304-5427, United States; orcid.org/0000-0001-8494-9325

Peng Ma – *Bio-Acoustic MEMS in Medicine (BAMM)*
Laboratory, Canary Center at Stanford for Cancer Early Detection, Department of Radiology, School of Medicine Stanford University, Palo Alto, California 94304-5427, United States; *Canary Center at Stanford for Cancer Early Detection, Department of Radiology, School of Medicine, Stanford University, Palo Alto, California 94304-5427, United States*

Rajib Ahmed – *Bio-Acoustic MEMS in Medicine (BAMM)*
Laboratory, Canary Center at Stanford for Cancer Early Detection, Department of Radiology, School of Medicine Stanford University, Palo Alto, California 94304-5427, United States; *Canary Center at Stanford for Cancer Early Detection, Department of Radiology, School of Medicine, Stanford University, Palo Alto, California 94304-5427, United States*; orcid.org/0000-0002-9184-2400

Huaxiao Yang – *Stanford Cardiovascular Institute, Stanford University, Palo Alto, California 94304-5427, United States*; Present Address: Department of Biomedical Engineering, University of North Texas, Denton, Texas, 76078, USA

Sihan Chen – *Department of Biomedical Engineering, Wuhan University School of Basic Medical Sciences, Wuhan 430071, China*; *Hubei Province Key Laboratory of Allergy and Immunology, Wuhan, Hubei 430071, China*

Jibo Wang – *Department of Biomedical Engineering, Wuhan University School of Basic Medical Sciences, Wuhan 430071, China*; *Hubei Province Key Laboratory of Allergy and Immunology, Wuhan, Hubei 430071, China*

Chun Liu – *Stanford Cardiovascular Institute, Stanford University, Palo Alto, California 94304-5427, United States*

Demir Akin – *Bio-Acoustic MEMS in Medicine (BAMM)*
Laboratory, Canary Center at Stanford for Cancer Early Detection, Department of Radiology, School of Medicine Stanford University, Palo Alto, California 94304-5427, United States; *Canary Center at Stanford for Cancer Early Detection, Department of Radiology, School of Medicine, Stanford University, Palo Alto, California 94304-5427, United States*

Kaiyu Fu – *Canary Center at Stanford for Cancer Early Detection, Department of Radiology, School of Medicine, Stanford University, Palo Alto, California 94304-5427, United States*; Department of Electrical Engineering, Stanford University, Stanford, California 94305, United States; orcid.org/0000-0002-7899-0388

Xu Cao – *Stanford Cardiovascular Institute, Stanford University, Palo Alto, California 94304-5427, United States*; orcid.org/0000-0002-8368-6727

Pu Chen – *Department of Biomedical Engineering, Wuhan University School of Basic Medical Sciences, Wuhan 430071, China*; *Hubei Province Key Laboratory of Allergy and Immunology, Wuhan, Hubei 430071, China*

En-Chi Hsu – *Canary Center at Stanford for Cancer Early Detection, Department of Radiology, School of Medicine, Stanford University, Palo Alto, California 94304-5427, United States*; Present Address: Institute of Molecular and Genomic Medicine, National Health Research Institutes, Zhunan, Miaoli 35053, Taiwan

Hyongsok Tom Soh – *Canary Center at Stanford for Cancer Early Detection, Department of Radiology, School of Medicine, Stanford University, Palo Alto, California 94304-*

5427, United States; Department of Electrical Engineering, Stanford University, Stanford, California 94305, United States; orcid.org/0000-0001-9443-857X

Tanya Stoyanova – Canary Center at Stanford for Cancer Early Detection, Department of Radiology, School of Medicine, Stanford University, Palo Alto, California 94304-5427, United States

Joseph C. Wu – Stanford Cardiovascular Institute, Stanford University, Palo Alto, California 94304-5427, United States

Complete contact information is available at:
<https://pubs.acs.org/10.1021/acsnano.2c01908>

Author Contributions

○Contribute equally to this work.

Notes

The authors declare no competing financial interest.

ACKNOWLEDGMENTS

We acknowledge the Canary Center at Stanford for Cancer Early Detection. F.S. was supported the Schmidt Science Fellows, in partnership with the Rhodes Trust.

REFERENCES

- (1) Li, Y.; Liu, X.; Xu, X.; Xin, H.; Zhang, Y.; Li, B. Red-Blood-Cell Waveguide as a Living Biosensor and Micromotor. *Adv. Funct. Mater.* **2019**, *29* (50), 1905568.
- (2) Xu, H.; Medina-Sánchez, M.; Magdanz, V.; Schwarz, L.; Hebenstreit, F.; Schmidt, O. G. Sperm-hybrid micromotor for targeted drug delivery. *ACS Nano* **2018**, *12* (1), 327–337.
- (3) Wei, X.; Beltrán-Gastélum, M.; Karshalev, E.; Esteban-Fernández de Avila, B.; Zhou, J.; Ran, D.; Angsantikul, P.; Fang, R. H.; Wang, J.; Zhang, L. Biomimetic micromotor enables active delivery of antigens for oral vaccination. *Nano Lett.* **2019**, *19* (3), 1914–1921.
- (4) Gao, W.; Dong, R.; Thamphiwatana, S.; Li, J.; Gao, W.; Zhang, L.; Wang, J. Artificial micromotors in the mouse's stomach: A step toward in vivo use of synthetic motors. *ACS Nano* **2015**, *9* (1), 117–123.
- (5) Xin, H.; Zhao, N.; Wang, Y.; Zhao, X.; Pan, T.; Shi, Y.; Li, B. Optically controlled living micromotors for the manipulation and disruption of biological targets. *Nano Lett.* **2020**, *20* (10), 7177–7185.
- (6) Wu, Z.; Li, T.; Li, J.; Gao, W.; Xu, T.; Christianson, C.; Gao, W.; Galarnyk, M.; He, Q.; Zhang, L.; Wang, J. Turning erythrocytes into functional micromotors. *ACS Nano* **2014**, *8* (12), 12041–12048.
- (7) Shao, J.; Xuan, M.; Zhang, H.; Lin, X.; Wu, Z.; He, Q. Chemotaxis-guided hybrid neutrophil micromotors for targeted drug transport. *Angew. Chem.* **2017**, *129* (42), 13115–13119.
- (8) Akolpoglu, M. B.; Dogan, N. O.; Bozuyuk, U.; Ceylan, H.; Kizilel, S.; Sitti, M. High-Yield Production of Biohybrid Microalgae for On-Demand Cargo Delivery. *Advanced Science* **2020**, *7* (16), 2001256.
- (9) Wang, H.; Pumera, M. Micro/nanomachines and living biosystems: from simple interactions to microcyborgs. *Adv. Funct. Mater.* **2018**, *28* (25), 1705421.
- (10) Magdanz, V.; Khalil, I. S. M.; Simmchen, J.; Furtado, G. P.; Mohanty, S.; Gebauer, J.; Xu, H.; Klingner, A.; Aziz, A.; Medina-Sanchez, M.; Schmidt, O. G.; Misra, S. IRONSperm: Sperm-templated soft magnetic microrobots. *Science advances* **2020**, *6* (28), eaba5855.
- (11) Wang, B.; Chan, K. F.; Yuan, K.; Wang, Q.; Xia, X.; Yang, L.; Ko, H.; Wang, Y.-X. J.; Sung, J. J. Y.; Chiu, P. W. Y.; Zhang, L. Endoscopy-assisted magnetic navigation of biohybrid soft microrobots with rapid endoluminal delivery and imaging. *Science Robotics* **2021**, *6* (52), DOI: 10.1126/scirobotics.abd2813.
- (12) Tang, S.; Zhang, F.; Gong, H.; Wei, F.; Zhuang, J.; Karshalev, E.; Esteban-Fernandez de Avila, B.; Huang, C.; Zhou, Z.; Li, Z.; Yin, L.; Dong, H.; Fang, R. H.; Zhang, X.; Zhang, L.; Wang, J. Enzyme-powered Janus platelet cell robots for active and targeted drug delivery. *Science Robotics* **2020**, *5* (43), DOI: 10.1126/scirobotics.a-ba6137.
- (13) Pacheco, M.; Jurado-Sánchez, B.; Escarpa, A. Visible-Light-Driven Janus Microvehicles in Biological Media. *Angew. Chem., Int. Ed.* **2019**, *58* (50), 18017–18024.
- (14) Sun, L.; Yu, Y.; Chen, Z.; Bian, F.; Ye, F.; Sun, L.; Zhao, Y. Biohybrid robotics with living cell actuation. *Chem. Soc. Rev.* **2020**, *49*, 4043.
- (15) Tanaka, Y.; Morishima, K.; Shimizu, T.; Kikuchi, A.; Yamato, M.; Okano, T.; Kitamori, T. An actuated pump on-chip powered by cultured cardiomyocytes. *Lab Chip* **2006**, *6* (3), 362–368.
- (16) Shin, S. R.; Jung, S. M.; Zalabany, M.; Kim, K.; Zorlutuna, P.; Kim, S. b.; Nikkhal, M.; Khabiry, M.; Azize, M.; Kong, J.; Wan, K.-t.; Palacios, T.; Dokmeci, M. R.; Bae, H.; Tang, X.; Khademhosseini, A. Carbon-nanotube-embedded hydrogel sheets for engineering cardiac constructs and bioactuators. *ACS Nano* **2013**, *7* (3), 2369–2380.
- (17) Shin, S. R.; Shin, C.; Memic, A.; Shadmehr, S.; Miscuglio, M.; Jung, H. Y.; Jung, S. M.; Bae, H.; Khademhosseini, A.; Tang, X. S.; Dokmeci, M. R. Aligned carbon nanotube-based flexible gel substrates for engineering biohybrid tissue actuators. *Adv. Funct. Mater.* **2015**, *25* (28), 4486–4495.
- (18) Park, J.; Kim, I. C.; Baek, J.; Cha, M.; Kim, J.; Park, S.; Lee, J.; Kim, B. Micro pumping with cardiomyocyte-polymer hybrid. *Lab Chip* **2007**, *7* (10), 1367–1370.
- (19) Yoon, J.; Eyster, T. W.; Misra, A. C.; Lahann, J. Cardiomyocyte-driven actuation in biohybrid microcylinders. *Adv. Mater.* **2015**, *27* (30), 4509–4515.
- (20) Chan, V.; Park, K.; Collens, M. B.; Kong, H.; Saif, T. A.; Bashir, R. Development of miniaturized walking biological machines. *Sci. Rep.* **2012**, *2* (1), 1–8.
- (21) Williams, B. J.; Anand, S. V.; Rajagopalan, J.; Saif, M. T. A. A self-propelled biohybrid swimmer at low Reynolds number. *Nat. Commun.* **2014**, *5* (1), 1–8.
- (22) Akiyama, Y.; Iwabuchi, K.; Furukawa, Y.; Morishima, K. Long-term and room temperature operable bioactuator powered by insect dorsal vessel tissue. *Lab Chip* **2009**, *9* (1), 140–144.
- (23) Akiyama, Y.; Sakuma, T.; Funakoshi, K.; Hoshino, T.; Iwabuchi, K.; Morishima, K. Atmospheric-operable bioactuator powered by insect muscle packaged with medium. *Lab Chip* **2013**, *13* (24), 4870–4880.
- (24) Chen, Z.; Fu, F.; Yu, Y.; Wang, H.; Shang, Y.; Zhao, Y. Cardiomyocytes-actuated Morpho butterfly wings. *Adv. Mater.* **2019**, *31* (8), 1805431.
- (25) Wang, H.; Liu, Y.; Chen, Z.; Sun, L.; Zhao, Y. Anisotropic structural color particles from colloidal phase separation. *Science advances* **2020**, *6* (2), eaay1438.
- (26) Xi, J.; Schmidt, J. J.; Montemagno, C. D. Self-assembled microdevices driven by muscle. *Nature materials* **2005**, *4* (2), 180–184.
- (27) Feinberg, A. W.; Feigel, A.; Shevkopyas, S. S.; Sheehy, S.; Whitesides, G. M.; Parker, K. K. Muscular thin films for building actuators and powering devices. *Science* **2007**, *317* (5843), 1366–1370.
- (28) Park, S.-J.; Gazzola, M.; Park, K. S.; Park, S.; Di Santo, V.; Blevins, E. L.; Lind, J. U.; Campbell, P. H.; Dauth, S.; Capulli, A. K.; Pasqualini, F. S.; Ahn, S.; Cho, A.; Yuan, H.; Maoz, B. M.; Vijaykumar, R.; Choi, J.-W.; Deisseroth, K.; Lauder, G. V.; Mahadevan, L.; Parker, K. K. Phototactic guidance of a tissue-engineered soft-robotic ray. *Science* **2016**, *353* (6295), 158–162.
- (29) Nawroth, J. C.; Lee, H.; Feinberg, A. W.; Ripplinger, C. M.; McCain, M. L.; Grosberg, A.; Dabiri, J. O.; Parker, K. K. A tissue-engineered jellyfish with biomimetic propulsion. *Nature biotechnology* **2012**, *30* (8), 792–797.
- (30) Cvetkovic, C.; Raman, R.; Chan, V.; Williams, B. J.; Tolish, M.; Bajaj, P.; Sakar, M. S.; Asada, H. H.; Saif, M. T. A.; Bashir, R. Three-dimensionally printed biological machines powered by skeletal muscle. *Proc. Natl. Acad. Sci. U. S. A.* **2014**, *111* (28), 10125–10130.

- (31) Raman, R.; Grant, L.; Seo, Y.; Cvetkovic, C.; Gapinske, M.; Palasz, A.; Dabbous, H.; Kong, H.; Pinera, P. P.; Bashir, R. Damage, healing, and remodeling in optogenetic skeletal muscle bioactuators. *Adv. Healthcare Mater.* **2017**, *6* (12), 1700030.
- (32) Pagan-Diaz, G. J.; Zhang, X.; Grant, L.; Kim, Y.; Aydin, O.; Cvetkovic, C.; Ko, E.; Solomon, E.; Hollis, J.; Kong, H.; Saif, T.; Gazzola, M.; Bashir, R. Simulation and fabrication of stronger, larger, and faster walking biohybrid machines. *Adv. Funct. Mater.* **2018**, *28* (23), 1801145.
- (33) Shang, Y.; Chen, Z.; Fu, F.; Sun, L.; Shao, C.; Jin, W.; Liu, H.; Zhao, Y. Cardiomyocyte-driven structural color actuation in anisotropic inverse opals. *ACS Nano* **2019**, *13* (1), 796–802.
- (34) Shum, A. M.; Che, H.; Wong, A. O. T.; Zhang, C.; Wu, H.; Chan, C. W.; Costa, K.; Khine, M.; Kong, C. W.; Li, R. A. A Micropatterned Human Pluripotent Stem Cell-Based Ventricular Cardiac Anisotropic Sheet for Visualizing Drug-Induced Arrhythmogenicity. *Adv. Mater.* **2017**, *29* (1), 1602448.
- (35) Matsudaira, K.; Takahashi, H.; Hirayama-Shoji, K.; Nguyen, T.-V.; Tsukagoshi, T.; Shimoyama, I. A MEMS-based measurement system for evaluating the force-length relationship of human induced pluripotent stem cell-derived cardiomyocytes adhered on a substrate. *Journal of Micromechanics and Microengineering* **2019**, *29* (5), 055003.
- (36) Abadi, P. P. S. S.; Garbern, J. C.; Behzadi, S.; Hill, M. J.; Tresback, J. S.; Heydari, T.; Eftehadi, M. R.; Ahmed, N.; Copley, E.; Aghaverdi, H.; Lee, R. T.; Farokhzad, O. C.; Mahmoudi, M. Engineering of mature human induced pluripotent stem cell-derived cardiomyocytes using substrates with multiscale topography. *Adv. Funct. Mater.* **2018**, *28* (19), 1707378.
- (37) Yalikhun, Y.; Noguchi, Y.; Kamamichi, N.; Tanaka, Y. *Atmospheric-Operable 3D Printed Walking Bio-Robot Powered by Muscle-Tissue of Earthworm*, 2018 IEEE/RSJ International Conference on Intelligent Robots and Systems (IROS), Madrid, Spain, Oct. 1–5, 2018; pp 7595–7600, DOI: 10.1109/IROS.2018.8594343.
- (38) Uesugi, K.; Shimizu, K.; Akiyama, Y.; Hoshino, T.; Iwabuchi, K.; Morishima, K. Contractile performance and controllability of insect muscle-powered bioactuator with different stimulation strategies for soft robotics. *Soft Robotics* **2016**, *3* (1), 13–22.
- (39) Wang, J.; Zhang, X.; Park, J.; Park, I.; Kilicarslan, E.; Kim, Y.; Dou, Z.; Bashir, R.; Gazzola, M. Computationally assisted design and selection of maneuverable biological walking machines. *Advanced Intelligent Systems* **2021**, *3* (5), 2000237.
- (40) Raman, R.; Cvetkovic, C.; Uzel, S. G.; Platt, R. J.; Sengupta, P.; Kamm, R. D.; Bashir, R. Optogenetic skeletal muscle-powered adaptive biological machines. *Proc. Natl. Acad. Sci. U. S. A.* **2016**, *113* (13), 3497–3502.
- (41) Raman, R.; Cvetkovic, C.; Bashir, R. A modular approach to the design, fabrication, and characterization of muscle-powered biological machines. *Nature protocols* **2017**, *12* (3), 519–533.
- (42) Kriegman, S.; Blackiston, D.; Levin, M.; Bongard, J. A scalable pipeline for designing reconfigurable organisms. *Proc. Natl. Acad. Sci. U. S. A.* **2020**, *117* (4), 1853–1859.
- (43) Guix, M.; Mestre, R.; Patiño, T.; De Corato, M.; Fuentes, J.; Zarpellon, G.; Sánchez, S. Biohybrid soft robots with self-stimulating skeletons. *Science Robotics* **2021**, *6* (53), eabe7577.
- (44) Zhang, F.; Mundaca-Urbe, R.; Gong, H.; Esteban-Fernandez de Avila, B.; Beltran-Gastelum, M.; Karshalev, E.; Nourhani, A.; Tong, Y.; Nguyen, B.; Gallot, M.; Zhang, Y.; Zhang, L.; Wang, J. A macrophage–magnesium hybrid biomotor: fabrication and characterization. *Adv. Mater.* **2019**, *31* (27), 1901828.
- (45) Fu, F.; Shang, L.; Chen, Z.; Yu, Y.; Zhao, Y. Bioinspired living structural color hydrogels. *Science Robotics* **2018**, *3* (16), eaar8580.
- (46) Sun, L.; Yu, Y.; Chen, Z.; Bian, F.; Ye, F.; Sun, L.; Zhao, Y. Biohybrid robotics with living cell actuation. *Chem. Soc. Rev.* **2020**, *49* (12), 4043–4069.
- (47) Aubin, H.; Nichol, J. W.; Hutson, C. B.; Bae, H.; Sieminski, A. L.; Crokek, D. M.; Akhyari, P.; Khademhosseini, A. Directed 3D cell alignment and elongation in microengineered hydrogels. *Biomaterials* **2010**, *31* (27), 6941–6951.
- (48) Matsunaga, Y. T.; Morimoto, Y.; Takeuchi, S. Molding cell beads for rapid construction of macroscopic 3D tissue architecture. *Advanced materials* **2011**, *23* (12), H90–H94.
- (49) Kang, H.-W.; Lee, S. J.; Ko, I. K.; Kengla, C.; Yoo, J. J.; Atala, A. A 3D bioprinting system to produce human-scale tissue constructs with structural integrity. *Nature biotechnology* **2016**, *34* (3), 312–319.
- (50) Murphy, S. V.; De Coppi, P.; Atala, A. Opportunities and challenges of translational 3D bioprinting. *Nature biomedical engineering* **2020**, *4* (4), 370–380.
- (51) Jia, W.; Gungor-Ozkerim, P. S.; Zhang, Y. S.; Yue, K.; Zhu, K.; Liu, W.; Pi, Q.; Byambaa, B.; Dokmeci, M. R.; Shin, S. R.; Khademhosseini, A. Direct 3D bioprinting of perfusable vascular constructs using a blend bioink. *Biomaterials* **2016**, *106*, 58–68.
- (52) Colosi, C.; Shin, S. R.; Manoharan, V.; Massa, S.; Costantini, M.; Barbetta, A.; Dokmeci, M. R.; Dentini, M.; Khademhosseini, A. Microfluidic bioprinting of heterogeneous 3D tissue constructs using low-viscosity bioink. *Advanced materials* **2016**, *28* (4), 677–684.
- (53) Miri, A. K.; Khalilpour, A.; Cecen, B.; Maharjan, S.; Shin, S. R.; Khademhosseini, A. Multiscale bioprinting of vascularized models. *Biomaterials* **2019**, *198*, 204–216.
- (54) Lepowsky, E.; Muradoglu, M.; Tasoglu, S. Towards preserving post-printing cell viability and improving the resolution: Past, present, and future of 3D bioprinting theory. *Bioprinting* **2018**, *11*, e00034.
- (55) Chen, P.; Luo, Z.; Güven, S.; Tasoglu, S.; Ganesan, A. V.; Weng, A.; Demirci, U. Microscale assembly directed by liquid-based template. *Advanced materials* **2014**, *26* (34), 5936–5941.
- (56) Bouyer, C.; Chen, P.; Güven, S.; Demirtaş, T. T.; Nieland, T. J.; Padilla, F.; Demirci, U. A bio-acoustic levitational (BAL) assembly method for engineering of multilayered, 3D brain-like constructs, using human embryonic stem cell derived neuro-progenitors. *Advanced materials* **2016**, *28* (1), 161–167.
- (57) Ren, T.; Steiger, W.; Chen, P.; Ovsianikov, A.; Demirci, U. Enhancing cell packing in buckyballs by acoustofluidic activation. *Biofabrication* **2020**, *12* (2), 025033.
- (58) Guo, F.; Mao, Z.; Chen, Y.; Xie, Z.; Lata, J. P.; Li, P.; Ren, L.; Liu, J.; Yang, J.; Dao, M.; Suresh, S.; Huang, T. J. Three-dimensional manipulation of single cells using surface acoustic waves. *Proc. Natl. Acad. Sci. U. S. A.* **2016**, *113* (6), 1522–1527.
- (59) Ren, T.; Chen, P.; Gu, L.; Ogut, M. G.; Demirci, U. Soft Ring-Shaped Cell-Robots with Simultaneous Locomotion in Batches. *Adv. Mater.* **2020**, *32* (8), 1905713.
- (60) Rohr, S. Role of gap junctions in the propagation of the cardiac action potential. *Cardiovascular research* **2004**, *62* (2), 309–322.
- (61) Appiah, C.; Arndt, C.; Siemsen, K.; Heitmann, A.; Staubitz, A.; Selhuber-Unkel, C. Living materials herald a new era in soft robotics. *Adv. Mater.* **2019**, *31* (36), 1807747.
- (62) Churko, J. M.; Garg, P.; Treutlein, B.; Venkatasubramanian, M.; Wu, H.; Lee, J.; Wessells, Q. N.; Chen, S.-Y.; Chen, W.-Y.; Chetal, K.; Mantalas, G.; Neff, N.; Jabart, E.; Sharma, A.; Nolan, G. P.; Salomonis, N.; Wu, J. C. Defining human cardiac transcription factor hierarchies using integrated single-cell heterogeneity analysis. *Nat. Commun.* **2018**, *9* (1), 1–14.
- (63) Burrige, P. W.; Matsa, E.; Shukla, P.; Lin, Z. C.; Churko, J. M.; Ebert, A. D.; Lan, F.; Diecke, S.; Huber, B.; Mordwinkin, N. M.; Plews, J. R.; Abilez, O. J.; Cui, B.; Gold, J. D.; Wu, J. C. Chemically defined generation of human cardiomyocytes. *Nat. Methods* **2014**, *11* (8), 855–860.
- (64) Melde, K.; Choi, E.; Wu, Z.; Palagi, S.; Qiu, T.; Fischer, P. Acoustic fabrication via the assembly and fusion of particles. *Adv. Mater.* **2018**, *30* (3), 1704507.
- (65) Melde, K.; Mark, A. G.; Qiu, T.; Fischer, P. Holograms for acoustics. *Nature* **2016**, *537* (7621), 518–522.
- (66) Li, Q.; Li, S.; Zhang, X.; Xu, W.; Han, X. Programmed magnetic manipulation of vesicles into spatially coded prototissue architectures arrays. *Nat. Commun.* **2020**, *11* (1), 232.
- (67) Tasoglu, S.; Diller, E.; Guven, S.; Sitti, M.; Demirci, U. Untethered micro-robotic coding of three-dimensional material composition. *Nat. Commun.* **2014**, *5* (1), 1–9.

- (68) Ren, L.; Nama, N.; McNeill, J. M.; Soto, F.; Yan, Z.; Liu, W.; Wang, W.; Wang, J.; Mallouk, T. E. 3D steerable, acoustically powered microswimmers for single-particle manipulation. *Science advances* **2019**, *5* (10), eaax3084.
- (69) Zhou, C.; Suematsu, N. J.; Peng, Y.; Wang, Q.; Chen, X.; Gao, Y.; Wang, W. Coordinating an Ensemble of Chemical Micromotors via Spontaneous Synchronization. *ACS Nano* **2020**, *14* (5), 5360–5370.
- (70) Villa, K.; Děkanovský, L.; Plutnar, J.; Kosina, J.; Pumera, M. Swarming of Perovskite-Like Bi₂WO₆ Microrobots Destroy Textile Fibers under Visible Light. *Adv. Funct. Mater.* **2020**, *30* (51), 2007073.
- (71) Kong, L.; Mayorga-Martinez, C. C.; Guan, J.; Pumera, M. Photocatalytic micromotors activated by UV to visible light for environmental remediation, micropumps, reversible assembly, transportation, and biomimicry. *Small* **2019**, *16* (27), 1903179.
- (72) Tu, J.; Gao, W. Spray-on magnetic skin for robotic actuation. *Science Robotics* **2020**, *5* (48), DOI: 10.1126/scirobotics.abf1390.
- (73) Xu, T.; Soto, F.; Gao, W.; Dong, R.; Garcia-Gradilla, V.; Magaña, E.; Zhang, X.; Wang, J. Reversible swarming and separation of self-propelled chemically powered nanomotors under acoustic fields. *J. Am. Chem. Soc.* **2015**, *137* (6), 2163–2166.
- (74) Yu, Y.; Yu, D.; Orme, C. A. Reversible, tunable, electric-field driven assembly of silver nanocrystal superlattices. *Nano Lett.* **2017**, *17* (6), 3862–3869.
- (75) Wang, Q.; Chan, K. F.; Schweizer, K.; Du, X.; Jin, D.; Yu, S. C. H.; Nelson, B. J.; Zhang, L. Ultrasound Doppler-guided real-time navigation of a magnetic microswarm for active endovascular delivery. *Science Advances* **2021**, *7* (9), eabe5914.
- (76) Du, X.; Yu, J.; Jin, D.; Chiu, P. W. Y.; Zhang, L. Independent Pattern Formation of Nanorod and Nanoparticle Swarms under an Oscillating Field. *ACS Nano* **2021**, *15* (3), 4429–4439.
- (77) Zhou, H.; Mayorga-Martinez, C. C.; Pané, S.; Zhang, L.; Pumera, M. Magnetically Driven Micro and Nanorobots. *Chem. Rev.* **2021**, *121* (8), 4999–5041.
- (78) Dong, Y.; Wang, L.; Yuan, K.; Ji, F.; Gao, J.; Zhang, Z.; Du, X.; Tian, Y.; Wang, Q.; Zhang, L. Magnetic Microswarm Composed of Porous Nanocatalysts for Targeted Elimination of Biofilm Occlusion. *ACS Nano* **2021**, *15* (3), 5056–5067.
- (79) Mozetic, P.; Giannitelli, S. M.; Gori, M.; Trombetta, M.; Rainer, A. Engineering muscle cell alignment through 3D bioprinting. *J. Biomed. Mater. Res., Part A* **2017**, *105* (9), 2582–2588.
- (80) Kai, D.; Prabhakaran, M. P.; Jin, G.; Ramakrishna, S. Guided orientation of cardiomyocytes on electrospun aligned nanofibers for cardiac tissue engineering. *J. Biomed. Mater. Res. Part B: Appl. Biomater.* **2011**, *98* (2), 379–386.
- (81) Au, H. T. H.; Cheng, I.; Chowdhury, M. F.; Radisic, M. Interactive effects of surface topography and pulsatile electrical field stimulation on orientation and elongation of fibroblasts and cardiomyocytes. *Biomaterials* **2007**, *28* (29), 4277–4293.
- (82) Takahashi, H.; Okano, T. Cell sheet-based tissue engineering for organizing anisotropic tissue constructs produced using micro-fabricated thermoresponsive substrates. *Adv. Healthcare Mater.* **2015**, *4* (16), 2388–2407.
- (83) Wu, Y.; Wang, L.; Guo, B.; Ma, P. X. Interwoven aligned conductive nanofiber yarn/hydrogel composite scaffolds for engineered 3D cardiac anisotropy. *ACS Nano* **2017**, *11* (6), 5646–5659.
- (84) Latif, N.; Sarathchandra, P.; Taylor, P.; Antoniw, J.; Brand, N.; Yacoub, M. Characterization of molecules mediating cell-cell communication in human cardiac valve interstitial cells. *Cell Biochem. Biophys.* **2006**, *45* (3), 255–264.
- (85) Zhang, X.; Chen, G.; Sun, L.; Ye, F.; Shen, X.; Zhao, Y. Claw-inspired microneedle patches with liquid metal encapsulation for accelerating incisional wound healing. *Chemical Engineering Journal* **2021**, *406*, 126741.
- (86) Gong, Y.; Chen, Z.; Yang, L.; Ai, X.; Yan, B.; Wang, H.; Qiu, L.; Tan, Y.; Witman, N.; Wang, W.; Zhao, Y.; Fu, W. Intrinsic color sensing system allows for real-time observable functional changes on human induced pluripotent stem cell-derived cardiomyocytes. *ACS Nano* **2020**, *14* (7), 8232–8246.
- (87) Sun, L.; Chen, Z.; Bian, F.; Zhao, Y. Bioinspired soft robotic caterpillar with cardiomyocyte drivers. *Adv. Funct. Mater.* **2020**, *30* (6), 1907820.
- (88) Tandon, N.; Cannizzaro, C.; Chao, P.-H. G.; Maidhof, R.; Marsano, A.; Au, H. T. H.; Radisic, M.; Vunjak-Novakovic, G. Electrical stimulation systems for cardiac tissue engineering. *Nature protocols* **2009**, *4* (2), 155–173.
- (89) Chan, V.; Asada, H. H.; Bashir, R. Utilization and control of bioactuators across multiple length scales. *Lab Chip* **2014**, *14* (4), 653–670.

Recommended by ACS

Untethered Single Cell Grippers for Active Biopsy

Qianru Jin, David H. Gracias, *et al.*

MAY 28, 2020
NANO LETTERS

READ 

MechanoBioTester: A Decoupled Multistimulus Cell Culture Device for Studying Complex Microenvironments *In Vitro*

Bryan D. James, Josephine B. Allen, *et al.*

MAY 08, 2020
ACS BIOMATERIALS SCIENCE & ENGINEERING

READ 

Predictive Biophysical Cue Mapping for Direct Cell Reprogramming Using Combinatorial Nanoarrays

Letao Yang, Ki-Bum Lee, *et al.*

MARCH 18, 2022
ACS NANO

READ 

Actinosomes: Condensate-Templated Containers for Engineering Synthetic Cells

Ketan A. Ganar, Siddharth Deshpande, *et al.*

AUGUST 10, 2022
ACS SYNTHETIC BIOLOGY

READ 

Get More Suggestions >